A novel approach to designing cylindrical-surface shim coils for a superconducting magnet of magnetic resonance imaging*

Liu Wen-Tao(刘文韬), Zu Dong-Lin(俎栋林)†, and Tang Xin(唐 昕)

Beijing Key Laboratory of Medical Physics and Engineering, IHIP of Physics School, Peking University, Beijing 100871, *China*

(Received 14 May 2009; revised manuscript received 8 June 2009)

For a superconducting magnet of magnetic resonance imaging (MRI), the novel approach presented in this paper allows the design of cylindrical gradient and shim coils of finite length. The method is based on identification of the weighting of harmonic components in the current distribution that will generate a magnetic field whose z-component follows a chosen spherical harmonic function. Mathematical expressions which relate the harmonic terms in the cylindrical current distribution to spherical harmonic terms in the field expansion are established. Thus a simple matrix inversion approach can be used to design a shim coil of any order pure harmonic. The expressions providing a spherical harmonic decomposition of the field components produced by a particular cylindrical current distribution are novel. A stream function was applied to obtain the discrete wire distribution on the cylindrical-surface. This method does not require the setting of the target-field points. The discussion referring to matrix equations in terms of condition numbers proves that this novel approach has no ill-conditioned problems. The results also indicate that it can be used to design cylindrical-surface shim coils of finite length that will generate a field variation which follows a particular spherical harmonic over a reasonably large-sized volume.

Keywords: active shimming, superconducting MRI magnet, target-field approach，harmonic coils

PACC: 8760I, 8760D, 4110, 0350D

1. Introduction

As is well known for a superconducting magnet of magnetic resonance imaging (MRI), the magnetic field inhomogeneity, $\Delta B_0/B_0$, over 50 cm-diameter sphere volume (DSV) must be controlled within a few parts per million. A superconducting MRI magnet includes a set of main coils,[1] a set of active shimming coils, and shielding coils. All coils are immerged in liquid helium. Although the theoretical homogeneity of the main magnetic field of the designed main coils is already within a few ppm,[1] there are several factors which compromise the ideal homogeneity. First there exists machining tolerance with the main coils. Second, it is impossible that the temperature coefficients of the wire and the frame of the coils are precisely the same. Third, the coils will deform because of expanding due to heat and shrinking due to cold down from room temperature to liquid helium temperature (4.2 K). Eventually each piece of the superconducting wires finds itself counterpoise positions under the interaction of the current flow and the magnetic field when the coils are excited by a current source power. Consequently, the magnetic field produced by the main coils will deviate a great deal from the designed field. Hence a set of harmonic coils as active shimming is prepared altogether along the main coils.

Romeo and Hoult[2] presented a full mathematical framework for designing shim coils on a cylindrical-surface for MRI. They used a spherical harmonic to expand the magnetic field over a diameter sphere volume (DSV) of interest into a series.[3,4] To improve the field homogeneity over this DSV, each shim coil, responsible for adjusting one such harmonic, needs to be tuned to annul the zonal and tesseral harmonic fields. By combining current elements from various shapes, such as loop arcs, ellipse arcs, etc., it can enhance the harmonic of interest but eliminate unnecessary harmonics. Unfortunately, the qualified volume calculated from this method is less than the desired specification, especially for higher-order harmonic shim coil design.

An alternative method to obtain considerably larger usable volumes is the 'target field' method proposed by Turner.[5,6] This method has no ill-conditioned problem because Fourier transforms have unique inverses. In the original target field approach,[5] there is no explicit constraint on coil

*Project supported by the National Natural Science Foundation of China (Grant No. 60871001).

†Corresponding author. E-mail: dlzu@pku.edu.cn

© 2010 Chinese Physical Society and IOP Publishing Ltd

length, which may result in unnecessarily long coils. Therefore, to restrict the coil length, Turner[6] developed his method further by adding a constraint that the current density must fall to zero outside of a finite interval. As a compromise it degrades the target field method as discussed by Jin.[7]

The design of cylindrical coils of finite length that will generate a field variation that follows a particular spherical harmonic over a reasonably-sized volume is particularly valuable. The pure spherical harmonic is orthonormal so there are no mutual inductances between such superconducting shim coils one another, and that allows the electric current in each shim coil to be independently adjusted. Mathematically, the compensation magnetic fields from these shim coils governed by the Biot–Savart law can be converted into a first-kind Fredholm integral equation to find the current density distribution. However, the integral equation cannot be solved essentially since it is a well-known ill-conditioned problem.

Crozier and Doddrell[8] also used simulated annealing as an optimization strategy to overcome the difficulty of finite length. Nevertheless, their method may require many iterations to converge and is thus time-consuming in terms of computation. Then, Forbes and Crozier generalized the integral equation of the target-field approach to design finite-length shim and gradient coils on a cylinder surface.[9,10] To overcome the ill-condition in the integral equation as mentioned above, they used a minimization technique combined with Tikhonov regularization to solve the current density on surfaces of zonal and tesseral shim coils. This method thus needs choosing of the regularization function and an abstract penalty function. However, these choices are at the discretion of designers. The Tikhonov regularization method likely shows a high superiority for designing asymmetrical shim coils. The linear programming algorithm for shim design[11] embodies much flexibility for an MRI magnet with complex geometry. Liu *et al.*[12] overcame this type of problem for gradient-coil design by selecting a collection of the target-field points properly instead of using Tikhonov regularization. Unfortunately this method seems invalid for designing higher order shim coils.

In this paper, we combine the conventional harmonics approach[2,4] and target-field approach[5,6,9,10,12] to design cylindrical-surface shim coils with finite length. To our knowledge, this is the first time that the relationship between a set of current density coefficients (corresponding to each order and each degree harmonic) and the harmonic field coefficient itself has been upbuilt.

2. Theory

As shown in Fig. 1, a field-point $\boldsymbol{r}$ is described by the spherical polar coordinate system $\boldsymbol{r}\,(r,\theta,\phi)$ or the cylindrical coordinate system $\boldsymbol{r}\,(\rho,\phi,z)$, while a source-point $\boldsymbol{r'}$ is described by the spherical polar coordinate system $\boldsymbol{r}\,'(f,\alpha,\psi)$ or the cylindrical-surface coordinate system $\boldsymbol{r'}\,(a,\psi,z')$.

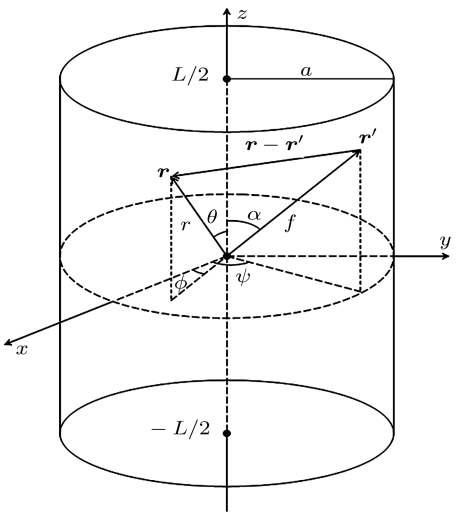


Fig. 1. A cylindrical coil with radius a and length L. A field-point coordinate $\boldsymbol{r}(r,\theta,\phi)$ and $\boldsymbol{r}(\rho,\phi,z)$, a source-point coordinate $\boldsymbol{r'}(f,\alpha,\psi)$ and $\boldsymbol{r'}(a,\psi,z')$ are shown, respectively.

For a finite length coil the current density components should be zero outside the interval $-L/2 < z < L/2$. We suppose that the components of the current density on the cylindrical-surface are able to be expanded as a Fourier series below:

$$\begin{cases} J_\psi = \cos(k\psi)\sum\limits_{q=1}^{Q} U_q\left[(1-\eta_{l+k})\sin\left(k_q z/2\right)+\eta_{l+k}\cos\left(k_q z\right)\right], \\ J_z = \sin(k\psi)\sum\limits_{q=1}^{Q}\dfrac{k}{a\,k_q}U_q\left[\eta_{l+k}\sin\left(k_q z\right)-2\left(1-\eta_{l+k}\right)\cos\left(k_q z/2\right)\right], \end{cases} \qquad \eta_x = \frac{1+(-1)^x}{2} = \begin{cases} 1 & x \text{ is even}, \\ 0 & x \text{ is odd}, \end{cases} \tag{1}$$

where l and k denote an order (corresponding to polar angle) and a degree (corresponding to azimuth angle) of a harmonic coil, respectively; $k_q = 2\pi q/L$, q is an integer; U_q are the Fourier coefficients of the current density expansion. The cylindrical-surface current density, $\boldsymbol{J} = J_\psi \hat{\boldsymbol{e}}_\psi + J_z \hat{\boldsymbol{e}}_z$ ($\hat{\boldsymbol{e}}_\psi$ and $\hat{\boldsymbol{e}}_z$ denote the unit vector in the ψ- and z-directions, respectively) satisfies the continuity equation $\nabla \cdot \boldsymbol{J} = 0$, which on the cylindrical surface can be written as

$$\frac{\partial J_\psi}{a\,\partial\psi} + \frac{\partial J_z}{\partial z} = 0. \tag{2}$$

The continuity equation for the current density on the coil surface with $\rho = a$ leads to the concept of a stream function, $S(\psi, z)$,[13] which satisfies

$$J_\psi = -\frac{\partial S}{\partial z}, \quad J_z = \frac{\partial S}{a\,\partial\psi}. \tag{3}$$

The stream function can be further shown as follows:

$$S(\psi, z) = \cos(k\psi)\sum_{q=1}^{Q}\frac{1}{k_q}U_q[2(1-\eta_{l+k})\cos(k_q z/2) - \eta_{l+k}\sin(k_q z)]. \tag{4}$$

Our aim is to find a relationship between the Fourier coefficients U_q of each order harmonic coil current and its corresponding order of spherical harmonic magnetic field. For this aim we will expand the Biot–Savart law in a Fourier–Legendre series. By the Biot–Savart formulas, the current density element vector $\boldsymbol{J}\,\mathrm{d}\sigma'$ at a source point $\boldsymbol{r}'(f, \alpha, \psi)$ on the cylindrical-surface will generate a magnetic induction vector $\mathrm{d}\boldsymbol{B}$ at a field point $\boldsymbol{r}(r, \theta, \phi)$ within the coil, thus

$$\mathrm{d}\boldsymbol{B} = \frac{\mu_0}{4\pi}\nabla\frac{1}{|\boldsymbol{r}-\boldsymbol{r}'|}\times\boldsymbol{J}\,\mathrm{d}\sigma', \tag{5}$$

where $\mathrm{d}\sigma' = a\,\mathrm{d}\psi\,\mathrm{d}z$ is an area element. Following the analysis of Romeo and Hoult[2] over a spherical region with radius $r < f_{\min} = a$, the Green's function $1/|\boldsymbol{r}-\boldsymbol{r}'|$ can be expanded into spherical harmonic series:

$$\frac{1}{|\boldsymbol{r}-\boldsymbol{r}'|} = \frac{1}{f}\sum_{n=0}^{\infty}\sum_{m=0}^{n}\varepsilon_m\frac{(n-m)!}{(n+m)!}P_{nm}(\cos\alpha)\left(\frac{r}{f}\right)^n P_{nm}(\cos\theta)\cos[m(\phi-\psi)], \quad \varepsilon_m = \begin{cases} 1 & m = 0, \\ 2 & m \neq 0, \end{cases} \tag{6}$$

where $P_{nm}(x)$ are Ferrer's associated Legendre polynomials of the nth order mth degree and $n \geq m \geq 0$. Substituting Eq. (6) into Eq. (5) and integrating it over the cylindrical-surface (see Appendix A), we can obtain the z-component of the magnetic induction field, $B_z(r, \theta, \phi)$, which is the dominant component of interest in MRI systems.

$$B_z = \sum_{n=0}^{\infty}\sum_{m=0}^{n} b_{nm} r^n P_{nm}(\cos\theta)\begin{pmatrix}\cos(m\phi)\\ \sin(m\phi)\end{pmatrix}, \tag{7}$$

where the expansion coefficients b_{nm} are given by

$$b_{nm} = \frac{\mu_0 a}{4\pi}\int_{-L/2}^{L/2}\mathrm{d}z\int_0^{2\pi}\mathrm{d}\psi\,\varepsilon_m C_{nm} J_\psi(\cos(m\psi)\ \sin(m\psi)), \tag{8}$$

with

$$C_{nm} = \frac{(n-m)!}{(n+m)!}\frac{1}{f^{n+2}}\frac{(n+1)P_{nm}(\cos\alpha) - (n-m+1)\cos\alpha P_{n+1,m}(\cos\alpha)}{\sin\alpha}, \tag{9}$$

and

$$\varepsilon_m = \begin{cases} 1, & m = 0, \\ 2, & m \neq 0, \end{cases} \qquad \begin{cases} f = \sqrt{a^2+z^2}, \\ \cos\alpha = z/\sqrt{a^2+z^2}. \end{cases} \tag{10}$$

To establish the relationship between the harmonic field coefficient b_{nm} and the corresponding harmonic coil current coefficient U_q, we define

$$j_\psi = \sum_{q=1}^{Q} U_q\left[(1-\eta_{l+k})\sin(k_q z/2) + \eta_{l+k}\cos(k_q z)\right]. \tag{11}$$

According to Eq. (1), we have

$$J_\psi = j_\psi \cos(k\psi). \tag{12}$$

By substituting Eq. (12) into Eq. (8), we obtain

$$b_{nm} = \frac{\mu_0 a}{4\pi} \int_{-L/2}^{L/2} \mathrm{d}z \int_0^{2\pi} \mathrm{d}\psi \ \varepsilon_m C_{nm} j_\psi (\cos(k\psi)\cos(m\psi) \ \ \cos(k\psi)\sin(m\psi)), \tag{13}$$

which can be further shown to be (see Appendix B)

$$b_{nm} = \mu_0 a \int_0^{L/2} \mathrm{d}z C_{nm} \delta_{km} \sum_{q=1}^{Q} U_q \left[(1-\eta_{n+m})(1-\eta_{l+k})\sin(k_q z/2) + \eta_{n+m}\eta_{l+k}\cos(k_q z)\right] \begin{pmatrix} 1 & 0 \end{pmatrix}. \tag{14}$$

From the definition of the Kronecker-delta symbol δ_{km}, we know that the lth order kth degree harmonic coil only generates a specific order and $m = k$ degree of harmonic magnetic field:

$$(B_z)_{nm} = b_{nm} r^n P_{nm}(\cos\theta)\cos(m\phi) \xrightarrow{\text{Let}} T_{nm}. \tag{15}$$

Other harmonics ($n \neq$ the specific number, $m \neq k$) are intrinsically zero. The relationship between the index n and l is slightly complex. By the nature of function η_x implied in Eq. (1), we carefully analyse the indices in Eq. (14). For non-zero harmonics we find that the index n not only relates l, but also k and an additional integer i. Hence we pick up those non-zero harmonics and arrange them with index i. The order n and degree m of the arrayed non-zero harmonics satisfy the following relationships:

$$m = k; \ n = k + (l+k) \bmod 2 + 2(i-1), \ i = 1, 2, \ldots. \tag{16}$$

Here the notation '$x \bmod y$' means to take the remainder of x divided by y. Thus, the weighting coefficient of the ith non-zero harmonic b_i can be expressed as:

$$\begin{aligned} b_i \ = \ b_{nk} &= \mu_0 a \int_0^{L/2} \mathrm{d}z \, C_{k+(l+k) \bmod 2+2(i-1),k} \\ &\times \sum_{q=1}^{Q} U_q \left[(1-\eta_{l+k})\sin(k_q z/2) + \eta_{l+k}\cos(k_q z)\right], \quad i = 1, 2, \ldots. \end{aligned} \tag{17}$$

Picking up the current coefficients U_q from the integral and for the first N non-zero harmonics ($i = 1, 2, \ldots N$), Eq. (17) can be rewritten into a matrix form: $\boldsymbol{b}(N \times 1) = \boldsymbol{D}(N \times Q)\boldsymbol{U}(Q \times 1)$. The elements of the coefficient matrix $\boldsymbol{D}(N \times Q)$ can be expressed as:

$$D(i,q) = \mu_0 a \int_0^{L/2} C_{k+(l+k) \bmod 2+2(i-1),k} \left[(1-\eta_{l+k})\sin(k_q z/2) + \eta_{l+k}\cos(k_q z)\right] \mathrm{d}z. \tag{18}$$

Given Eqs. (9) and (16), $C_{k+(l+k) \bmod 2+2(i-1),k}$ in Eqs. (17) and (18) can be shown to be equal to

$$\begin{aligned} & C_{k+(l+k) \bmod 2+2(i-1),k} \\ = \ & \frac{[k+(l+k) \bmod 2 + 2(i-1) - k]\,!}{[k+(l+k) \bmod 2 + 2(i-1) + k]\,!} \frac{1}{f^{k+(l+k) \bmod 2+2(i-1)+2}} \frac{1}{\sin\alpha} \\ & \times \{[k+(l+k) \bmod 2 + 2(i-1) + 1] P_{k+(l+k) \bmod 2+2(i-1),k}(\cos\alpha) \\ & - [k+(l+k) \bmod 2 + 2(i-1) - k + 1] \cos\alpha \cdot P_{k+(l+k) \bmod 2+2(i-1)+1,k}(\cos\alpha)\}. \end{aligned} \tag{19}$$

Thus, the general magnetic field expressed by Eq. (7) is rewritten as follows:

$$B_z = \sum_{i=1}^{N} \sum_{q=1}^{Q} U_q D(i,q) \, r^{k+(l+k) \bmod 2+2(i-1)} P_{k+(l+k) \bmod 2+2(i-1),k}(\cos\theta)\cos(k\phi). \tag{20}$$

From Eqs. (15)–(18) and (20), we have

$$b_i = b_{k+(l+k) \bmod 2+2(i-1),k} = \sum_{q=1}^{Q} U_q D(i,q) \xrightarrow{\text{Let}} A_i, \quad i = 1, 2, \ldots, N, \tag{21}$$

where $b_{k+(l+k) \bmod 2+2(i-1),k}$ is the weighting coefficient of the $[k+(l+k) \bmod 2+2(i-1)]$th order, the kth degree harmonic field, and is also the coefficient of the ith non-zero harmonic field:

$$\begin{aligned}&(B_z)_{k+(l+k) \bmod 2+2(i-1),k}\\ &= b_{k+(l+k) \bmod 2+2(i-1),k} r^{k+(l+k) \bmod 2+2(i-1)} P_{k+(l+k) \bmod 2+2(i-1),k}(\cos\theta)\cos(k\phi).\end{aligned} \tag{22}$$

N and Q may be chosen based on the accuracy required and the availability of computer resources. To generate a desired magnetic field, it needs to find an azimuthal current density component $J_\psi(\psi, z)$ on the coil surface with radius a and length L. If $U_q\,(q = 1, 2, \ldots, Q)$ is found, $J_\psi(\psi, z)$ and $J_z(\psi, z)$ become known as well based on Eq. (1). In fact in the harmonic field coefficient vector

$$\boldsymbol{A} = \begin{bmatrix} A_1 & A_2 & \ldots & A_N \end{bmatrix}^{\mathrm{T}}, \tag{23}$$

there is only one nonzero element, which represents a pure harmonic field. Note that in Eq.(23) superscript 'T' represents transpose, the subscript integer N meets the condition: $Q \geq N \geq (l-k)/2+1$. Equation (21) can be shown in its matrix format (i.e. $\boldsymbol{DU} = \boldsymbol{A}$) and $\boldsymbol{U}$ can be obtained as

$$\boldsymbol{U} = \boldsymbol{D}^{-1}\boldsymbol{A}. \tag{24}$$

When a target harmonic field coefficient is specified, the corresponding current coefficients can be found with the aid of a standard matrix solution routine. Then, we use the stream function method[13] to obtain the discrete wire distribution on the cylindrical surface.

3. Method

As a general demonstration of how to apply the theory above to design a shim coil, we take l and k as the order and degree of the desired coil respectively and denote the target shim coefficient as $b_{l,k}^{\mathrm{Target}}$. According to the analyses of Eq. (14), not all the orders and degrees of the harmonics will be generated by this coil. So we can simplify the design by picking up the non-zero harmonics and arraying them with the index i. The order n and degree m of each harmonics can be determined by Eq. (16). For each non-zero harmonics, it can be given a target coefficient A_i, then a target vector $\boldsymbol{A} = \begin{bmatrix} A_1 & A_2 & \cdots & A_N \end{bmatrix}^{\mathrm{T}}$ will be formed. Only one harmonic $T_{l,k}$ is desired among all these non-zero harmonics so we should find out the index i of $T_{l,k}$, set its coefficient A_i to be the target value $b_{l,k}^{\mathrm{Target}}$, and set other coefficients to be zero. To illustrate how to set a target harmonic field coefficient vector $\boldsymbol{A}$, we will discuss a few typical cases as follows.

Case 1 For a linear z-gradient coil with target gradient strength G_z, the target field is written as $B_z = G_z r P_{10}(\cos\theta)$, with $n = 1$ and $m = 0$. Thus the order of the z-gradient coil should be set as $l = 1$ and the degree $k = 0$. From Eq. (16), $n = 1+2(i-1)$, $i = 1, 2, 3, \ldots$. This type of coil includes not only zonal harmonic T_{10}, but also T_{30}, T_{50}, ..., in which the harmonic coefficients are A_1, A_2, A_3, ..., respectively. Therefore, to design a T_{10} shim coil with target coefficient G_z, we should set $A_1 = G_z$ and other harmonic coefficients $A_2 = 0, A_3 = 0, \ldots, A_N = 0$. In summary, the target harmonic field coefficient vector should be set as $\boldsymbol{A} = \begin{bmatrix} G_z & 0 & \cdots & 0 \end{bmatrix}^{\mathrm{T}}$, where we use G_z instead of b_{10}^{Target}(the first harmonics as shown in Table 1 in the first row) because b_{10}^{Target} is the linear z-gradient strength G_z.

Case 2 For a quadratic order zonal harmonic field $(B_z)_{20} = b_{20}^{\mathrm{Target}} r^2 P_{20}(\cos\theta)$ with $n = 2$ and $m = 0$, the order of the harmonic coil should be set as $l = 2$ and the degree $k = 0$. As required by Eq. (16), $n = 0, 2, 4, \ldots$, this type of coil can generate zonal harmonics of T_{00}, T_{20}, T_{40}, ..., in which the harmonic coefficients are A_1, A_2, A_3, ..., respectively. Correspondingly we set the target harmonic field coefficient vector as $\boldsymbol{A} = \begin{bmatrix} 0 & b_{20}^{\mathrm{Target}} & 0 & \ldots & 0 \end{bmatrix}^{\mathrm{T}}$.

Case 3 For a cubic order tesseral harmonic field $(B_z)_{31} = b_{31}^{\mathrm{Target}} r^3 P_{31}(\cos\theta)\cos\phi$ with $n = 3$ and $m = 1$. The order of the shim coils should be set as $l = 3$ and the degree $k = 1$. Based on Eq. (16), $n = 1+2(i-1)$, $i = 1, 2, 3, \ldots$ (we can set $n = 1, 3, 5, \ldots$). This type of coil can generate harmonics T_{11}, T_{31}, T_{51}, ... To design a T_{31} shim coil we should set the target harmonic field coefficient vector as $\boldsymbol{A} = \begin{bmatrix} 0 & b_{31}^{\mathrm{Target}} & 0 & \ldots & 0 \end{bmatrix}^{\mathrm{T}}$. If designing a T_{11} shim coil the target harmonic field coefficient vector should be set as $\boldsymbol{A} = \begin{bmatrix} b_{11}^{\mathrm{Target}} & 0 & 0 & \ldots & 0 \end{bmatrix}^{\mathrm{T}}$. Note that the coefficient b_{11}^{Target} is the linear transversal gradient G_x.

More cases of non-zero harmonics for some types of coil are listed in Table 1. Numerical simulation was carried out in Matlab (The Mathworks, Inc., Natick,

MD, USA). The spherical harmonics were divided into two subsets,[2,9,10] zonal ($m = 0$) and tesseral ($m \neq 0$) harmonics. Any pure zonal shim coils and half of the tesseral shim coils can be directly designed using the procedures set up here. The other half of the tesseral shim coils can be obtained by rotating their counterparts with a proper angle (to be discussed later). Provided the geometry parameters for the cylinder shim coil corresponding to the lth order kth degree harmonic $b_{l,k}^{\text{Target}}$ are given, we can compute the current density coefficients U_q of the lth order kth degree harmonic coil according to these formulae set up above. Then the stream function $S(\psi, z)$ in Eq. (4) will be calculated. Finally, the winding patterns of the coils can be directly obtained by contouring the stream function.

Table 1. Non-zero harmonics and target vector setting for some types of coil.

coil type: (l,k)	non-zero harmonics	target vector setting as example
(1, 0)	$T_{1,0}, T_{3,0}, T_{5,0}, T_{7,0}, T_{9,0}, \ldots$	$\left[b_{1,0}^{\text{Target}}, 0, 0, 0, \ldots, 0\right]^{\text{T}}$
(1, 1)	$T_{1,1}, T_{3,1}, T_{5,1}, T_{7,1}, T_{9,1}, \ldots$	$\left[b_{1,1}^{\text{Target}}, 0, 0, 0, \ldots, 0\right]^{\text{T}}$
(2, 0)	$T_{0,0}, T_{2,0}, T_{4,0}, T_{6,0}, T_{8,0}, \ldots$	$\left[0, b_{2,0}^{\text{Target}}, 0, 0, \ldots, 0\right]^{\text{T}}$
(2, 1)	$T_{2,1}, T_{4,1}, T_{6,1}, T_{8,1}, T_{10,1}, \ldots$	$\left[b_{2,1}^{\text{Target}}, 0, 0, 0, \ldots, 0\right]^{\text{T}}$
(2, 2)	$T_{2,2}, T_{4,2}, T_{6,2}, T_{8,2}, T_{10,2}, \ldots$	$\left[b_{2,2}^{\text{Target}}, 0, 0, 0, \ldots, 0\right]^{\text{T}}$
(3, 0)	$T_{1,0}, T_{3,0}, T_{5,0}, T_{7,0}, T_{9,0}, \ldots$	$\left[0, b_{3,0}^{\text{Target}}, 0, 0, \ldots, 0\right]^{\text{T}}$
(3, 1)	$T_{1,1}, T_{3,1}, T_{5,1}, T_{7,1}, T_{9,1}, \ldots$	$\left[0, b_{3,1}^{\text{Target}}, 0, 0, \ldots, 0\right]^{\text{T}}$
(3, 2)	$T_{3,2}, T_{5,2}, T_{7,2}, T_{9,2}, T_{11,2}, \ldots$	$\left[b_{3,2}^{\text{Target}}, 0, 0, 0, \ldots, 0\right]^{\text{T}}$
(3, 3)	$T_{3,3}, T_{5,3}, T_{7,3}, T_{9,3}, T_{11,3}, \ldots$	$\left[b_{3,3}^{\text{Target}}, 0, 0, 0, \ldots, 0\right]^{\text{T}}$
(4, 0)	$T_{0,0}, T_{2,0}, T_{4,0}, T_{6,0}, T_{8,0}, \ldots$	$\left[0, 0, b_{4,0}^{\text{Target}}, 0, \ldots, 0\right]^{\text{T}}$
(4, 1)	$T_{2,1}, T_{4,1}, T_{6,1}, T_{8,1}, T_{10,1}, \ldots$	$\left[0, b_{4,1}^{\text{Target}}, 0, 0, \ldots, 0\right]^{\text{T}}$
(4, 2)	$T_{2,2}, T_{4,2}, T_{6,2}, T_{8,2}, T_{10,2}, \ldots$	$\left[0, b_{4,2}^{\text{Target}}, 0, 0, \ldots, 0\right]^{\text{T}}$
(4, 3)	$T_{4,3}, T_{6,3}, T_{8,3}, T_{10,3}, T_{12,3}, \ldots$	$\left[b_{4,3}^{\text{Target}}, 0, 0, 0, \ldots, 0\right]^{\text{T}}$
(4, 4)	$T_{4,4,}, T_{6,4}, T_{8,4}, T_{10,4}, T_{12,4}, \ldots$	$\left[b_{4,4}^{\text{Target}}, 0, 0, 0, \ldots, 0\right]^{\text{T}}$

4. Results

Figures 2(a)–6(a) show the coil winding patterns of the harmonics T_{20}, T_{21}, T_{22}, T_{30}, T_{40} respectively obtained with our method. In these examples, the coil length was set to be $L = 1.2$ m and its radius was $a = 0.6$ m. The target field is located over a 0.5 m DSV. In these figures the solid lines and the dashed lines represent the forward windings and reverse windings, respectively. The magnetic component B_z produced by the harmonics T_{20}, T_{21}, T_{22}, T_{30} and T_{40} shim coils, as a function of (x, z) or (x, y) are shown in (b) and (c) of Figs. 2–6, respectively. These spherical harmonics are evaluated at the target region of a 0.5 m DSV. In (b) and (c) of Figs. 2–6, most of the harmonic fields B_z produced by shim coils were found to show excellent agreement with the ideal harmonic fields. In these figures, thick dashed lines represent the ideal harmonic field as a reference. The thin solid lines represent the field produced by the designed current-carried coils. In some figures near the boundaries of the imaging region there are noticeable deviations, which are caused either by discretization of current densities or by not large enough Q values in Eqs. (1), (4), (20), and (21). For a larger Q the coil can produce a shim field exactly equal to the ideal harmonic field. However, the increase in Q also leads to more frequent mathematical oscillation of the current density. Figure 4 in Ref. [12] shows the cases with $Q = 6$ and $Q = 10$. The counteraction of the field caused by the frequently reversed current necessarily reduces the efficiency of the coils and increases the

difficulty in manufacturing. Therefore, a compromise must be made between accuracy and efficiency. When the index numbers Q are chosen with propriety, the current density just does not appear to have mathematical oscillation and meets the target field with reasonable accuracy. The efficiency for $T_{l,k}$ shimming coils is defined as:

$$\text{Efficiency} = b_{l,k}/I_0, \tag{25}$$

where $b_{l,k}$ is the order l and degree k harmonic coefficient of the generated field when current I_0 is flowing in the wires. Table 2 also includes terms of efficiency for typical $T_{l,k}$ shimming coils. These results show that the novel method for design shim coils allows decomposition of field harmonics into harmonic coefficients. To design a cylinder shim coil with a finite length, given any harmonic coefficient $b_{l,k}$, the pure harmonic coil corresponding to the $b_{l,k}$ could be computed easily and efficiently.

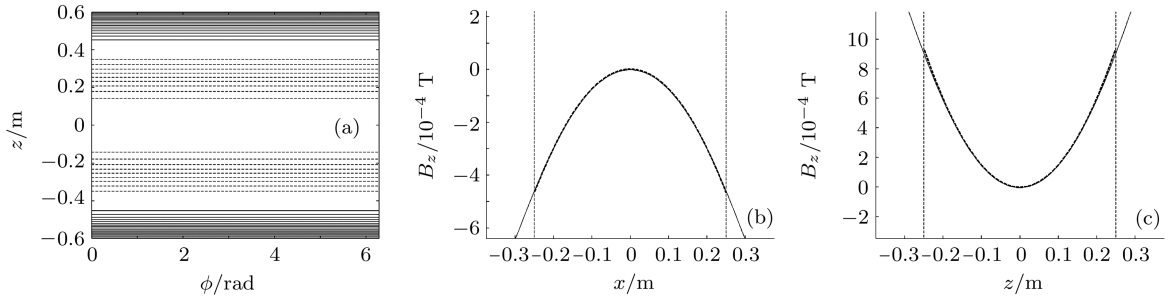


Fig. 2. Zonal harmonic T_{20}. (a) The winding pattern, with dashed lines representing reverse winding. The fields B_z produced by T_{20} along the z-axis and the x-axis are shown in (b) and (c), respectively, where the thick dashed lines are the ideal harmonics and the vertical dashed lines indicate the DSV boundary. Discretization during the calculation causes the errors close to the boundary in (c).

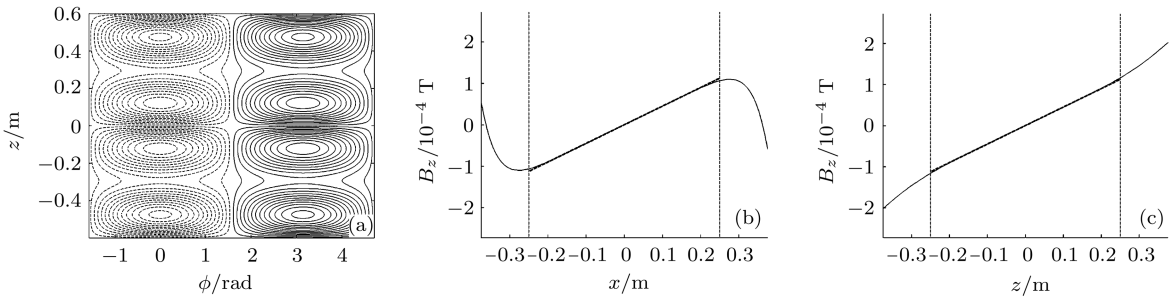


Fig. 3. Tesseral harmonic T_{21}. (a) The winding pattern, with the dashed lines representing reverse windings. The fields B_z produced by T_{21} along the z-axis and the x-axis are shown in (b) and (c), respectively, where the thick dashed lines represent the ideal harmonic field and the two vertical dashed lines indicate the boundary of the imaging region. The linearity (gradient) of the field in the target region is clearly shown in (b) and (c).

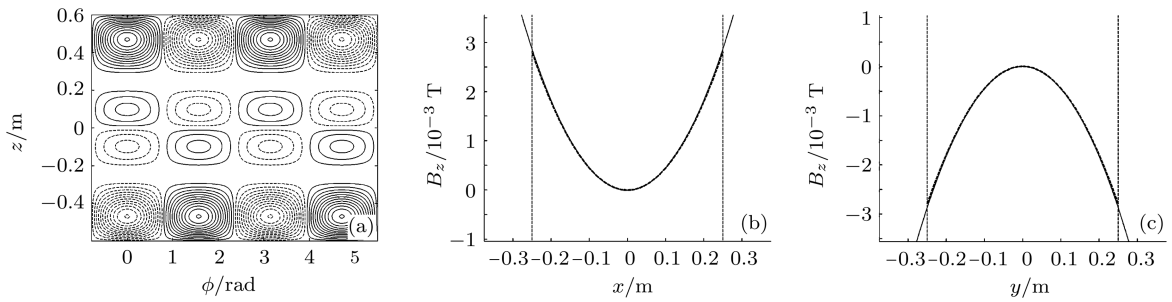


Fig. 4. T_{22} shim coil. (a) The winding pattern, with the dashed lines representing reverse windings. The fields B_z produced by T_{22} along the z-axis and the y-axis are shown in (b) and (c), respectively, where the thick dashed lines represent the ideal harmonic field and the two vertical dashed lines indicate the boundary of the imaging region.

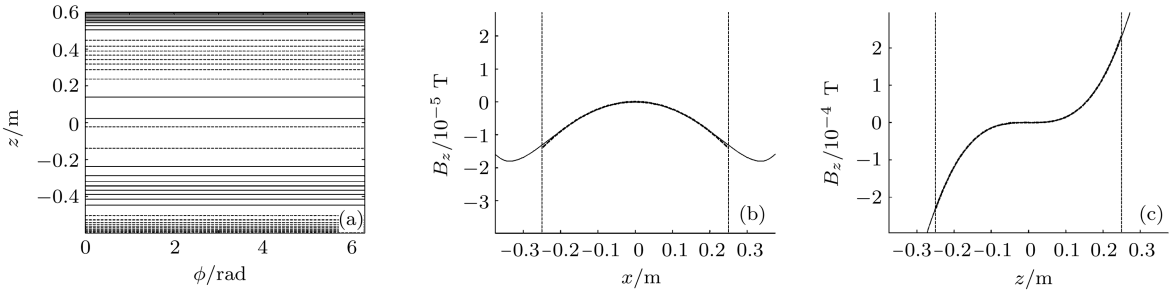


Fig. 5. Zonal T_{30} shim coil. (a) The winding pattern, with the dashed lines representing reverse windings. The fields B_z produced by T_{30} along the x-axis and the z-axis are shown in (b) and (c), respectively, where the thick dashed lines represent the ideal harmonic field and the two vertical dashed lines indicate the boundary of the imaging region.

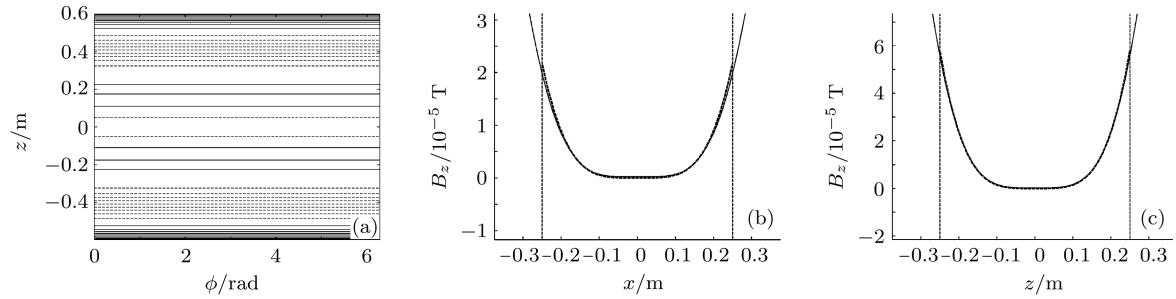


Fig. 6. Zonal T_{40} shim coil. (a) The winding pattern, with the dashed lines representing reverse windings. The fields B_z produced by T_{40} along the x-axis and the z-axis are shown in (b) and (c), respectively, where the thick dashed lines represent the ideal harmonic field and the two vertical dashed lines indicate the boundary of the imaging region.

Unlike Eq. (7), Eqs. (15) and (20) only include harmonics associated with $\cos(k\phi)$ but $\sin(k\phi)$. As they are orthogonal to one another, we assume $T_{l,k}$ and $T'_{l,k}$ represent shim coils associated with $\cos(k\phi)$ and $\sin(k\phi)$, respectively. For example, harmonic fields $T_{21} = b_{21}r^2P_{21}(\cos\theta)\cos\phi$ and $T'_{21} = b_{21}r^2P_{21}(\cos\theta)\sin\phi$ are orthogonal to each other. The $T_{l,k}$ shim coils can be designed directly using the above expressions and then T'_{21} can be obtained by rotating the T_{21} shim coil through 90 degrees. The same way, the T'_{31} shim coil can be obtained by rotating the T_{31} shim coil through 90 degrees. Analogically rotating by 45 degrees transforms T_{22} and T_{32} shim coils into T'_{22} and T'_{32}, respectively; rotating by 30 degrees transforms T_{33} shim coil into T'_{33}. In other words the other half of the tesseral harmonics coils can be obtained by simply rotating their counterparts. It is feasible and convenient to use the current density solved using the above equations for all terms and rotate them to obtain shim terms not covered by the equations. The aspect ratio ($L/D = 1$) of the shim coils is set quite small as samples in this paper. Such a method done here facilitates the design of super-short MRI superconducting magnets. Although the difficulty of designing pure harmonic shim coils is increased as a compromise, not bad results are obtained already.

Table 2. The data associated with design for these shim coils shown in Figs. 2–6.

coil type	T_{20}	T_{21}	T_{22}	T_{30}	T_{40}
chosen Q	3	3	3	3	4
Cond ($\boldsymbol{D}$)	120	126	37.7	1740	4255
$\kappa_{\max}$	4.6	18.1	17.5	4.4	3.6
efficiency	6.25×10^{-5} T/m^2/A	6.5×10^{-6} T/m^2/A	9.1×10^{-6} T/m^2/A	4.51×10^{-5} T/m^3/A	4.70×10^{-5} T/m^4/A
time taken	0.562 s	1.200 s	1.133 s	0.606 s	0.962 s

5. Discussion

The coils designed here had the fewest negative currents or highest power efficiency for the Q chosen in Eqs. (1), (4), and (21). Compared with other standard methods[12] this new method shows remarkable advantages. Firstly, this method is well conditioned since it has no poor conditioning problems. To test this point we can analyse the condition number of $\boldsymbol{D}$, $\mathrm{Cond}(\boldsymbol{D}) = \|\boldsymbol{D}\| \left\|\boldsymbol{D}^{-1}\right\|$, a degree of ill-condition, in Eq. (24). Derived from Eq. (24), we have $\|\Delta \boldsymbol{U}\|/\|\boldsymbol{U}\| \leq \|\boldsymbol{D}\| \left\|\boldsymbol{D}^{-1}\right\| \|\Delta \boldsymbol{A}\|/\|\boldsymbol{A}\|$.[14] For different Q in Eq. (21), the $\mathrm{Cond}(\boldsymbol{D})$ is different. The optimal Q and $\mathrm{Cond}(\boldsymbol{D})$ for these typical design cases are listed in Table 2.

For the worst case of the T_{40} shim coil with $Q = 4$, the maximum of $\mathrm{Cond}(\boldsymbol{D})$ is 4255. In this case, Eq. (24) has

$$\boldsymbol{D} = \begin{bmatrix} 28.87 & 16.72 & -6.941 & -1.474 \\ -3.477 & -9.152 & -10.98 & -5.291 \\ 0.2122 & 1.400 & 2.735 & 2.835 \\ -0.004943 & -0.09986 & -0.3342 & -0.6080 \end{bmatrix} \times 10^{-3}, \quad \boldsymbol{A} = \begin{bmatrix} 0 \\ 0 \\ 1 \\ 0 \end{bmatrix}, \quad \boldsymbol{U} = \begin{bmatrix} 17.36 \\ -23.52 \\ 16.74 \\ -5.484 \end{bmatrix} \times 10^{3}, \tag{26}$$

giving $\boldsymbol{A}$ a random deviation $\Delta \boldsymbol{A}$, the ratio of the fractional deviation of $\boldsymbol{U}$ to $\boldsymbol{A}$ is,

$$\kappa = \frac{\|\Delta \boldsymbol{U}\|/\|\boldsymbol{U}\|}{\|\Delta \boldsymbol{A}\|/\|\boldsymbol{A}\|}. \tag{27}$$

For 10^6 random calculations, when $\Delta \boldsymbol{A} = [-0.0004 \quad -0.0015 \quad -0.0095 \quad -0.0324]^{\mathrm{T}}$ and $\|\Delta \boldsymbol{A}\|/\|\boldsymbol{A}\| \leq 12\%$, the maximum of κ is $\kappa_{\max} = 3.608$, and $\kappa_{\max} \ll \mathrm{Cond}(\boldsymbol{D})$. This suggests that a small change in $\boldsymbol{A}$ will not result in a significant variation in $\boldsymbol{U}$.

Secondly, this new method could acquire a much more stable solution than our previous method.[12] For example, using the target-field method[12] to design a T_{20} shim coil by setting 7 target points over a DSV, the $\mathrm{Cond}(\boldsymbol{D})$ is $1.1 \times 10^{+11}$. Even with $\|\Delta \boldsymbol{A}\|/\|\boldsymbol{A}\| \leq 12\%$, for 10^6 random calculations, the maximum of κ is still $\kappa_{\max} = 1.9 \times 10^{+10}$. However, to design the same T_{20} shim coil using the new method by setting $Q = 4$, the $\mathrm{Cond}(\boldsymbol{D})$ is $4.3 \times 10^{+3}$. With $\|\Delta \boldsymbol{A}\|/\|\boldsymbol{A}\| \leq 12\%$, for 10^6 random calculations, the maximum of κ is $\kappa_{\max} = 28$, which is more acceptable compared with $1.9 \times 10^{+10}$. Hence our target-field method published in Ref. [12] is only used to design MRI gradient coils. The reason for the new method being more stable than the target field method is that the target vector $\boldsymbol{A}$ here has only one nonzero element, while in the other method each element of the target vector $\boldsymbol{A}$, magnetic induction at each target field point, cannot be zero generally. Mathematically in this new method, the normalized vectors $\boldsymbol{A}$ form the orthogonal base-vector in Hilbert space and are unshakable theoretically. The poor-conditioning of an equation is limited not only by the bad conditioning of the coefficient matrix, but also by the target vector $\boldsymbol{A}$. As such, for some special vector domains, the final equation shows no poor conditioning problem, even if the coefficient matrix is badly conditioned. In this paper, the vector $\boldsymbol{A}$ for each type of shim coil is set to a target value and cannot be arbitrarily changed according to the principle. As the $\boldsymbol{A}$ is fixed, in the calculation $\Delta \boldsymbol{A}$ is only caused by the imprecise computer mantissa. However, in MATLAB (where our numerical simulations were carried out) the accuracy is 2.204×10^{-16}. So even when $\boldsymbol{A}$ contains 10^2 elements, $\|\Delta \boldsymbol{A}\|/\|\boldsymbol{A}\|$ is not likely to be larger than 1×10^{-14}. According to Table 2, the maximum $\mathrm{Cond}(\boldsymbol{D})$ is less than 10^5, so $\|\Delta \boldsymbol{U}\|/\|\boldsymbol{U}\|$ is absolutely less than 10^{-9}. It obviously has nothing to do with the accuracy of the solution. Therefore the solution is stable and there are no ill-conditioned problems.

Because the Q are not very large (less than 6) and N is not larger than Q, the coefficient matrices are in a small scale, and the calculations are not very time consuming. For example, designing a T_{20} shim coil using our new method with $Q = 3$, $\mathrm{Cond}(\boldsymbol{D}) = 120$, and $\|\Delta \boldsymbol{A}\|/\|\boldsymbol{A}\| \leq 12\%$, for 1000000 times of random calculation (the maximum of κ is $\kappa_{\max} = 4.6$), the computation time is only 0.562 s on our Intel E8200 with 4 G memory computer. In order to be clear, the

computation times for typical $T_{l,k}$ shimming coils are listed in the lowest line of Table 2.

6. Conclusion

A new analytical methodology has been developed by combining the conventional harmonics[2,4] and current target-field approaches.[5,6,9,10,12] A matrix equation relating the field harmonics expressed by harmonic coefficients $b_{l,k}$, and the unknown current density expressed by a Fourier series with weighting coefficients U_q has been established. All orders and degrees of cylindrical-surface shim coils of finite length for a superconducting MRI scanner can be designed by the procedures established in this paper. This method does not require the setting of the target-field points. The discussion referring to matrix equations in terms of condition numbers proves that the governing matrix equation is better conditioned and has no ill-conditioned problems. The designing results also prove the novel method to be valid and efficient. The novel method renders the design of a pure harmonic shim coil simple and straightforward. Except for static shimming, it is also useful in dynamic shimming because its calculation time is short.

Appendix A

The magnetic induction field produced by the current element is referred to in Fig. A1. The relationship between the magnetic induction vector $\mathrm{d}\boldsymbol{B}$ at a field point $\boldsymbol{r}\,(r,\theta,\phi)$ within the coil and the current density element vector $\boldsymbol{J}\,\mathrm{d}\sigma'$ at a source point $\boldsymbol{r}'\,(f,\alpha,\psi)$ on a cylindrical-surface is given by the Biot–Savart law

$$\mathrm{d}\boldsymbol{B} = \frac{\mu_0}{4\pi}\nabla\frac{1}{|\boldsymbol{r}-\boldsymbol{r}'|}\times\boldsymbol{J}\,\mathrm{d}\sigma', \tag{A1}$$

where $\mathrm{d}\sigma' = a\,\mathrm{d}\psi\,\mathrm{d}z$ is an area element. It is well known that over the region with $r < f_{\min} = a$, the Green's function $1/|\boldsymbol{r}-\boldsymbol{r}'|$ can be expanded[2] in a spherical harmonic series:

$$\frac{1}{|\boldsymbol{r}-\boldsymbol{r}'|} = \frac{1}{f}\sum_{n=0}^{\infty}\sum_{m=0}^{n}\varepsilon_m\frac{(n-m)!}{(n+m)!}P_{nm}(\cos\alpha)\left(\frac{r}{f}\right)^n P_{nm}(\cos\theta)\cos[m(\phi-\psi)],\quad \varepsilon_m = \begin{cases}1 & m=0,\\ 2 & m\neq 0.\end{cases} \tag{A2}$$

For clarity, we let

$$\boldsymbol{A} = \nabla\frac{1}{|\boldsymbol{r}-\boldsymbol{r}'|}. \tag{A3}$$

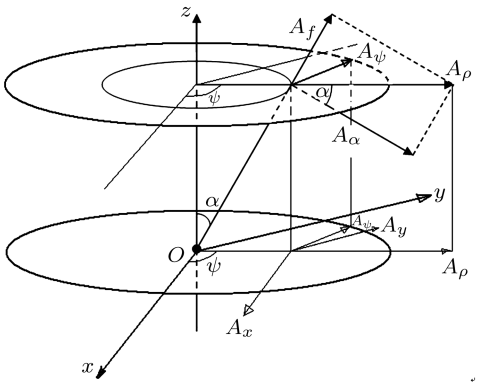


Fig. A1. The geometrical nexus among the spherical polar coordinate components A_f, A_α, the cylindrical coordinate component A_ρ, A_ψ and Cartesian coordinate component A_x, A_y, at an arbitrary point within the coil.

For a cylindrical-surface coil with radius a, the coordinates of the current on the cylindrical-surface satisfy $a = f\sin\alpha$ and $z = f\cos\alpha$ (see Fig. A1). Here we only consider the z-component and use coordinate transformation between the Cartesian and spherical coordinates; refer to Fig. A1, thus,

$$\nabla\frac{1}{|\boldsymbol{r}-\boldsymbol{r}'|}\times\boldsymbol{J}\cdot\hat{\boldsymbol{e}}_z$$
$$= \boldsymbol{A}\times\boldsymbol{J}\cdot\hat{\boldsymbol{e}}_z = A_xJ_y - A_yJ_x$$

$$
\begin{aligned}
&= (A_\rho \cos\psi - A_\psi \sin\psi) J_y - (A_\rho \sin\psi + A_\psi \cos\psi) J_x \\
&= [(A_f \sin\alpha + A_\alpha \cos\alpha)\cos\psi - A_\psi \sin\psi] J_\psi \cos\psi - [(A_f \sin\alpha + A_\alpha \cos\alpha)\sin\psi + A_\psi \cos\psi](-J_\psi \sin\psi) \\
&= (A_f \sin\alpha + A_\alpha \cos\alpha) J_\psi . \qquad \text{(A4)}
\end{aligned}
$$

Thus, according to Eq. (A1) the z-component of the magnetic induction field is:

$$
\mathrm{d}B_z = \frac{\mu_0}{4\pi}\mathrm{d}\sigma' A_\rho J_\psi = \frac{\mu_0}{4\pi}\mathrm{d}\sigma' (A_f \sin\alpha + A_\alpha \cos\alpha) J_\psi . \qquad \text{(A5)}
$$

In spherical coordinates, $\nabla = \dfrac{\partial}{\partial r}\hat{\boldsymbol{e}}_r + \dfrac{1}{r}\dfrac{\partial}{\partial\theta}\hat{\boldsymbol{e}}_\theta + \dfrac{1}{r\sin\theta}\dfrac{\partial}{\partial\phi}\hat{\boldsymbol{e}}_\phi$[15] and $\nabla\dfrac{1}{|\boldsymbol{r}-\boldsymbol{r}'|} = -\nabla'\dfrac{1}{|\boldsymbol{r}-\boldsymbol{r}'|}$; thus,

$$
A_f = -\frac{\partial}{\partial f}\frac{1}{|\boldsymbol{r}-\boldsymbol{r}'|} = \sum_{n=0}^{\infty}\sum_{m=0}^{n}\varepsilon_m \frac{(n-m)!}{(n+m)!}\frac{r^n}{f^{n+2}} P_{nm}(\cos\theta)(n+1) P_{nm}(\cos\alpha)\cos(m(\phi-\psi)), \qquad \text{(A6)}
$$

$$
A_\alpha = -\frac{1}{f}\frac{\partial}{\partial\alpha}\frac{1}{|\boldsymbol{r}-\boldsymbol{r}'|} = -\sum_{n=0}^{\infty}\sum_{m=0}^{n}\varepsilon_m \frac{(n-m)!}{(n+m)!}\frac{r^n}{f^{n+2}} P_{nm}(\cos\theta)\frac{\partial P_{nm}(\cos\alpha)}{\partial\alpha}\cos(m(\phi-\psi)). \qquad \text{(A7)}
$$

Substituting them into (A5), we obtain

$$
\begin{aligned}
\mathrm{d}B_z =& \frac{\mu_0}{4\pi}\mathrm{d}\sigma' \sum_{n=0}^{\infty}\sum_{m=0}^{n}\varepsilon_m \frac{(n-m)!}{(n+m)!}\frac{r^n}{f^{n+2}} P_{nm}(\cos\theta) J_\psi \\
&\times \left[(n+1)\sin\alpha P_{nm}(\cos\alpha) - \cos\alpha\frac{\partial P_{nm}(\cos\alpha)}{\partial\alpha}\right]\cos(m(\phi-\psi)). \qquad \text{(A8)}
\end{aligned}
$$

Note that the z-component of the field only involves the azimuthal component J_ψ of the current density vector. However, this is related to the axial component J_z through the continuity equation (2). In order to separate the field and the source variables, we let

$$
\begin{aligned}
C_{nm} &= \frac{(n-m)!}{(n+m)!}\frac{1}{f^{n+2}}\left[(n+1)\sin\alpha P_{nm}(\cos\alpha) - \cos\alpha\frac{\partial P_{nm}(\cos\alpha)}{\partial\alpha}\right] \\
&= \frac{(n-m)!}{(n+m)!}\frac{1}{f^{n+2}}\frac{(n+1)P_{nm}(\cos\alpha) - (n-m+1)\cos\alpha P_{n+1,m}(\cos\alpha)}{\sin\alpha}. \qquad \text{(A9)}
\end{aligned}
$$

The calculus operation concerning Ferrer's associated Legendre polynomials may refer to Ref. [15]. Thus, Eq. (A5) is recast as

$$
\begin{aligned}
\mathrm{d}B_z &= \frac{\mu_0}{4\pi}\mathrm{d}\sigma' \sum_{n=0}^{\infty}\sum_{m=0}^{n}\varepsilon_{\mathrm{m}} C_{nm} r^n P_{nm}(\cos\theta) J_\psi(\cos(m\phi)\cos(m\psi) + \sin(m\phi)\sin(m\psi)) \\
&= \frac{\mu_0}{4\pi}\mathrm{d}\sigma' \sum_{n=0}^{\infty}\sum_{m=0}^{n}\varepsilon_m C_{nm} r^n P_{nm}(\cos\theta) J_\psi (\cos(m\psi)\ \ \sin(m\psi))\begin{pmatrix}\cos(m\phi)\\ \sin(m\phi)\end{pmatrix}. \qquad \text{(A10)}
\end{aligned}
$$

We define a two-component expression:

$$
b_{nm} = \frac{\mu_0 a}{4\pi}\int_{-L/2}^{L/2}\mathrm{d}z\int_0^{2\pi}\mathrm{d}\psi\ \varepsilon_m C_{nm} J_\psi(\cos(m\psi)\ \ \sin(m\psi)). \qquad \text{(A11)}
$$

Thus,

$$
B_z = \sum_{n=0}^{\infty}\sum_{m=0}^{n} b_{nm} r^n P_{nm}(\cos\theta)\begin{pmatrix}\cos(m\phi)\\ \sin(m\phi)\end{pmatrix}. \qquad \text{(A12)}
$$

Appendix B

According to the orthogonality of the trigonometric function

$$\begin{aligned}
&\int_0^{2\pi} \sin k\psi \sin(m\psi)\,\mathrm{d}\psi = (\varepsilon_m - 1)\,\pi\delta_{k,m},\\
&\int_0^{2\pi} \cos k\psi \cos(m\psi)\,\mathrm{d}\psi = 2\pi\delta_{k,m}/\varepsilon_m,\\
&\int_0^{2\pi} \sin k\psi \cos(m\psi)\,\mathrm{d}\psi = 0,
\end{aligned} \tag{B1}$$

where $\delta_{k,m}$ is the Kronecker δ-function, Eq. (13) is simplified to

$$\begin{aligned}
b_{nm} &= \frac{\mu_0 a}{4\pi}\int_{-L/2}^{L/2} \mathrm{d}z\varepsilon_m C_{nm} j_\psi \begin{pmatrix} 2\pi\delta_{k,m}/\varepsilon_m & 0 \end{pmatrix}\\
&= \frac{\mu_0 a}{2}\int_{-L/2}^{L/2} \mathrm{d}z C_{nm}\delta_{k,m} j_\psi \begin{pmatrix} 1 & 0 \end{pmatrix}.
\end{aligned} \tag{B2}$$

Inserting Eq. (11) into Eq. (B2) we have

$$b_{nm} = \frac{\mu_0 a}{2}\int_{-L/2}^{L/2} \mathrm{d}z C_{nm}\delta_{k,m}\sum_{q=1}^{Q} U_q\left[(1-\eta_{l+k})\sin(k_q z/2) + \eta_{l+k}\cos(k_q z)\right]\begin{pmatrix} 1 & 0 \end{pmatrix}. \tag{B3}$$

The line integral in Eq. (B3) can be disconnected as two terms:

$$\begin{aligned}
&= \frac{\mu_0 a}{2}\int_0^{L/2} \mathrm{d}z C_{nm}(z)\,\delta_{k,m}\sum_{q=1}^{Q} U_q\left[(1-\eta_{l+k})\sin(k_q z/2) + \eta_{l+k}\cos(k_q z)\right]\begin{pmatrix} 1 & 0 \end{pmatrix}\\
&\quad + \frac{\mu_0 a}{2}\int_{-L/2}^{0} \mathrm{d}(-z) C_{nm}(-z)\,\delta_{k,m}\sum_{q=1}^{Q} U_q\left[(1-\eta_{l+k})\sin(-k_q z/2) + \eta_{l+k}\cos(-k_q z)\right]\begin{pmatrix} 1 & 0 \end{pmatrix}.
\end{aligned} \tag{B4}$$

Applying the parity of the associated Legendre function:[15]

$$P_{nm}(-\cos\alpha) = (-1)^{n+m} P_{nm}(\cos\alpha), \tag{B5}$$

and noting that $f = \sqrt{a^2+z^2}, \cos\alpha = z/\sqrt{a^2+z^2}$, and according to Eq. (9) we have[15]

$$\begin{aligned}
C_{nm}(-z) &= \frac{(n-m)!}{(n+m)!}\frac{1}{f^{n+2}}\frac{(n+1)P_{nm}(-\cos\alpha) - (n-m+1)(-\cos\alpha)P_{n+1,m}(-\cos\alpha)}{\sin\alpha}\\
&= (-1)^{n+m} C_{nm}(z).
\end{aligned} \tag{B6}$$

Inserting Eq. (B6) into Eq. (B4), we obtain

$$b_{nm} = \mu_0 a\int_0^{L/2} \mathrm{d}z C_{nm}\delta_{k,m}\sum_{q=1}^{Q} U_q\left[(1-\eta_{n+m})(1-\eta_{l+k})\sin(k_q z/2) + \eta_{n+m}\eta_{l+k}\cos(k_q z)\right]\begin{pmatrix} 1 & 0 \end{pmatrix}. \tag{B7}$$

References

[1] Zu D L, Guo H, Song X Y and Bao S L 2002 *Chin. Phys.* **11** 1008

[2] Romeo F and Hoult D I 1984 *Magn. Reson. Med.* **1** 44

[3] Morse P M and Feshbach H 1953 *Methods of Theoretical Physics* (New York: McGraw-Hill)

[4] Golay M J E 1958 *Rev. Sci. Instru.* **29** 313

[5] Turner R 1986 *J. Phys.* D: *Appl. Phys.* **19** 147

[6] Turner R 1994 *Electrical Coils* US Patent 5289151

[7] Jin J M 1999 *Electromagnetic Analysis and Design in Magnetic Resonance Imaging* (Boca Raton, Fla.: CRC Press)

[8] Crozier S and Doddrell D M 1993 *J. Magn. Reson.* A **103** 354

[9] Forbes L K and Crozier S 2001 *J. Phys.* D: *Appl. Phys.* **34** 3447

[10] Forbes L K and Crozier S 2002 *J. Phys.* D: *Appl. Phys.* **35** 839

[11] Ungersma S E and Xu H 2004 *Magn. Reson. Med.* **52** 619

[12] Liu W, Zu D, Tang X and Guo H 2007 *J. Phys.* D: *Appl. Phys.* **40** 4418

[13] Tomasi D 2001 *Magn. Reson. Med.* **45** 505

[14] Atkinson K E 1978 *An Introduction to Numerical Analysis* (New York: Wiley) p458

[15] Abramowitz M and Stegun I 1972 *Handbook of Mathematical Functions)* (New York: Dover Publications)